Invited paper at the Second Symposium on Low Temperature Electronics and High Temperature Superconductivity, Electrochemical Society Meeting, Honolulu, Hawaii, May 17-21,1993

HIGH TEMPERATURE SUPERCONDUCTOR JOSEPHSON WEAK LINKS

B. D. Hunt, J. B. Barner, M. C. Foote, and R. P. Vasquez
Center for Space Microelectronics Technology, Jet Propulsion Laboratory,
California Institute of Technology, Pasadena,CA91109

High T_c edge-geometry SNS microbridges have been fabricated using ion-damaged $YBa_2Cu_3O_{7-x}$ (YBCO) and a nonsuperconducting phase of YBCO (N-YBCO) as normal metals. Optimization of the ion milling process used for YBCO edge formation and cleaning has resulted in ion-damage barrier devices which exhibit I-V characteristics consistent with the Resistively-Shunted-Junction (RSJ) model, with typical current densities (J_c) of= 5 x 10^6 A/cm^2 at 4.2 K. Characterization of N-YBCO films suggests that N-YBCO is the orthorhombic YBCO phase with oxygen disorder suppressing T_c. Weak links using N-YBCO as the normal metal show RSJ I-V characteristics and exponential scaling of J_c, with a normal metal coherence length of ≈ 23 Å. In behavior similar to that reported for grain boundary junctions, the N-YBCO I_cR_n products scale as $J_c^{0.84}$ for current densities below 10^5 A/cm^2. For both types of devices, typical I_cR_n products at 4.2 K are limited to 1 -2 mV at the highest current densities, possibly due to self-shielding effects.

INTRODUCTION

High temperature superconductor (HTS) Josephson devices are potentially useful for a variety of applications including high speed digital logic, Thz frequency sources and detectors, and sensitive magnetometers. One promising approach to HTS Josephson device fabrication is the use of superconductor/normal-metal/superconductor (SNS) microbridges. Such weak links generally possess nonhysteretic current-voltage (I-V) characteristics, which are well-suited for high speed logic and magnetometer applications. In addition, the utilization of a normal metal bridge can relax the severe bridge length constraints of an all-superconducting microbridge. This approach also allows control of J_c and R_n over a broad range simply by varying the normal metal bridge length.

There are a number of possible device geometries for fabrication of HTS SNS weak links including planar SNS microbridges (1,2,3,4), step-edge SNS weak links (5,6,7), sandwich-geometry SNS trilayers (8,9,10,1 1,12), and edge-geometry SNS weak links (13,14,15,16,17,18,19,20). This work focuses on epitaxial edge-geometry SNS weak links due to advantages associated with this approach. A schematic diagram of an edge geometry SNS weak link is shown in Figure 1. The basic device structure consists of a c-axis-oriented YBCO base electrode with an exposed edge. An epitaxial normal metal is deposited on the YBCO edge, followed by deposition of the YBCO counterelectrode. Because the top surface of the base electrode is covered by a thick insulator, electrical contact between the YBCO electrodes is confined to the edge of the lower YBCO film.

The principal advantages of the edge geometry include the facts that the critical N/S interfaces are located on the longer coherence length YBCO surfaces, current flow is along the high J_c direction parallel to the a-b planes throughout the device, and very small device areas can be produced using conventional photolithography. The edge geometry also enables very short microbridge lengths to be achieved and controlled, because the bridge length is determined by the deposited normal metal thickness. Edge junction

fabrication is somewhat simpler than for trilayer SNS devices, because the counter-electrode serves as the wiring layer and no additional insulator and wiring depositions are needed. A possible drawback of the edge geometry approach is that the ion milling process used to define the base electrode edge may cause YBCO surface damage. In addition, optimal device performance requires formation of tapered YBCO edges (discussed below). Because typical tapered edge fabrication processes produce YBCO edges with a single orientation, circuit layout can be more complex with these devices.

One of the most important factors in determining high T_c SNS device performance is the choice of which normal metal to incorporate in the device structure. In an all-epitaxial weak link, the normal metal must be lattice-matched to YBCO in order to provide a template for overgrowth of the counterelectrode. Two very important, but difficult requirements are that the normal metal be chemically compatible with YBCO at the counterelectrode growth temperature, and that the normal metal film should grow without thin spots or pinholes. A long normal metal coherence length is also desirable, 'and theoretical arguments suggest that the normal metal resistivity-coherence length product ($\rho_n\xi_n$) should be larger than the corresponding product for YBCO (21). These requirements severely restrict possible normal metal choices for HTS epitaxial weak links. This work examines new results with two different weak link barrier layers that meet at least some of the above constraints: ion-damaged YBCO layers and a nonsuperconducting phase of YBCO (15,16). Special attention is paid to optimization of the edge formation and edge cleaning processes, which are closely related to the ion-damaged weak links. The primary goals of this work were to develop a reliable and reproducible HTS device process, and to obtain improved HTS SNS device performance. As will be seen below, good results have been achieved using both weak link materials. However, additional improvements are still needed for some device applications, and strategies for further optimization will be discussed.

DEVICE FABRICATION

Details of the edge-geometry weak link fabrication process have been described previously (15,16,1 8,22), but will be briefly summarized here. Device fabrication begins with pulsed laser deposition of a c-axis-oriented YBCO thin film, typically on a $LaAlO_3$ substrate. Following growth of the base electrode, a thin (100-200 Å) MgO or cubic zirconia passivation layer is deposited over the YBCO before removal from the laser ablation chamber. Next a thick (6000-9000 Å) MgO layer is patterned using photolithography and liftoff. The patterned MgO film is utilized as an ion milling mask to produce a tapered edge in the YBCO base electrode, followed by a low energy ion cleaning step. This edge formation process is discussed in greater detail below. Just after cleaning of the YBCO edge, within the same vacuum system, the normal metal layer and YBCO counterelectrode are deposited at the appropriate growth temperatures. A lithography-ion milling step is then used to pattern via holes down to the base YBCO film and liftoff Au contact pads. Finally, another lithography-milling process defines the counterelectrode. Completed devices have counterelectrode widths ranging from 6 μm down to 1.5 μm.

EDGE CLEANING OPTIMIZATION AND ION-DAMAGED-YBCO WEAK LINKS

One of the most critical steps of edge-geometry weak link fabrication is the YBCO edge formation and cleaning process. The two key requirements for formation of the YBCO edge are: 1) that the edge must be tapered to prevent grain boundary formation in

the YBCO counterelectrode (23), and 2) that surface damage on the YBCO base electrode surface is minimized. Tapered YBCO edges are produced by Ar ion milling at an approximately 30° angle from the substrate surface (16). This angled ion milling edge cutting step is followed by a low energy ion cleaning step at normal incidence to the substrate surface. Both the edge cutting and edge cleaning steps are done in a turbo-pumped load-lock attached to the main laser ablation chamber. Between these two steps the device chip is transferred from one fixture to another inside the vented load lock under flowing N_2 gas, so that any air-exposure is minimal.

It is important to minimize ion surface damage on the YBCO base electrode edge, because such damage can result in a suppression of the energy gap in the YBCO film at the YBCO-normal metal interface, leading to a reduction of the device I_cR_n product. Edge surface damage may also result in a degradation of the quality of epitaxial overgrowth of the normal metal and counterelectrode layers. The degraded layer on the YBCO base electrode is caused by ion darnage during the edge cutting and edge cleaning steps, and presumably consists of both crystalline defects and stoichiometry shifts associated with preferential ion sputtering. Shifts in oxygen stoichiometry due to oxygen loss and oxygen disorder may be especially serious problems at the YBCO-normal metal interface due to the relatively high mobility of oxygen in YBCO (24). The thickness of the YBCO damage layer is related to the energy of the impinging ions and their angle of incidence. However, it is probably not correct to simply equate the damage layer thickness with the incident ion range, because some damage may anneal out during heating in oxygen for the counterelectrode growth, and also because oxygen disordering may extend deeper than the primary ion damage depth.

In order to investigate the effect of edge ion milling and cleaning parameters, we have examined the electrical properties of devices produced with no deposited normal metal layer, where the counterelectrode is deposited directly on the ion-milled YBCO base electrode edge. These experiments were done in an effort to optimize the edge junction cleaning procedure for application to devices with deposited normal metals, and also to investigate whether high quality, controllable weak links could be produced using an ion-damaged YBCO surface layer as a "normal metal". In fact, some of the first devices fabricated without deposited normal metal layers showed excellent electrical performance, as shown in the 77 K I-V characteristics of Figure 2(a). For this weak link, the YBCO edge was produced by Ar-ion-milling at 500 eV at 30" from the substrate surface, followed by a 50 eV normal incidence Ar ion cleaning step. This device has a current density of= 5×10^4 A/cm^2 at 77 K with an I_cR_n product of 153 μV and an R_nA product of 2.9×10^{-9} Ω-cm^2. The I-V characteristics are qualitatively consistent with the Resistively-Shunted-Junction (RSJ) model, although the devices on this chip do typically exhibit excess currents. The microwave response of this device is shown in Figure 2(b). Clean ac Josephson steps are seen in response to 14.4 GHz microwave irradiation with amplitudes that modulate as expected with increasing microwave power. These initial results encouraged us to investigate ion-damaged barrier weak links in more detail to see whether reproducible and controllable weak links could be produced in this manner.

As part of this study, a set of ion-damage barrier chips was fabricated using 500 eV Ar ions to etch tapered YBCO edges, followed by a normal-incidence Ar ion clean at ion energies ranging from 50 to 500 eV. The weak link electrical parameters J_c, I_cR_n, and R_nA were measured as a function of Ar ion cleaning energy. For these experiments the cleaning times were adjusted so that at each ion energy, the same total areal dose of 1.9×10^{17} ions/cm^2 was used. Figure 3 shows the dependence of the average value of J_c

on ion beam cleaning energy for four different device chips. The data shows a decrease in J_c with increasing cleaning energy up to 250 eV, as might be expected if the damage depth scales with ion range in the YBCO. However, at 500 eV, the average current density increases to a value close to that seen for the 50 eV cleaning case. This effect is not understood at this time. One point to note is that, although some variation is seen in J_c as the cleaning energy is varied, the total variation in J_c is not large. The other notable fact here is that the devices of Figure 3 exhibited RSJ-like I-V characteristics and ac Josephson steps only for cleaning energies less than or equal to 250 eV. Devices on the chip fabricated using 500 eV Ar ion cleaning showed flux-flow I-V characteristics at all temperatures and no ac Josephson steps under microwave irradiation. The lack of Josephson behavior in the 500 eV-cleaned devices probably indicates that the ion damage depth exceeds the superconducting coherence length.

The dependence of I_cR_n on the ion cleaning energy at 77 K is shown in Figure 4. The average I_cR_n products are roughly independent of cleaning energy below 250 eV, but drop off at the highest cleaning energy. The average I_cR_n values are $\approx$ 250 μV for the lower cleaning energies, but range up to $\approx$ 450 μV for some devices. These I_cR_n products are some of the highest reported for SNS weak links at 77 K. The average R_nA products for these chips were lowest for the 50 eV and 500 eV cleans, and highest at 250 eV, ranging from 3 x 10^{-10} to 1.7 x 10^{-9} Ω-cm^2 at 77 K. Overall, the best device and cleaning results were obtained using 50 eV Ar cleaning in combination with the 500 eV Ar edge milling step. At 4.2 K, under these conditions, for four chips (30 devices) the average J_c was 5.5 x 10^6 A/cm^2 with a standard deviation of 4.7 x 10^6 A/cm^2, the average R_nA product was 5.4 x 10^{-10} Ω-cm^2 with a standard deviation of 6.4 x 10^{-10} Ω-cm^2, and the average I_cR_n product was 1.03 mV with a standard deviation of 0.24 mV. Possible self-shielding limitations on I_cR_n are discussed in the next section. Other variations in the YBCO edge formation and cleaning process were also examined, including xenon cleaning, eliminating the ion cleaning step, and varying the edge ion mill etching energy. These process variations produced devices with parameters comparable to the weak links made using 500 eV Ar edge cutting and 50 eV Ar cleaning.

The basic conclusions of the edge formation studies are relevant to YBCO edge cleaning for application to SNS devices with deposited normal metals, as well as to fabrication of ion-damaged-YBCO SNS devices. From a cleaning perspective, the high current densities and low R_nA products found with the 50 eV Ar process indicate that this process produces very clean YBCO edges that should work well as growth templates for epitaxial normal metal devices. However, we do believe that further cleaning optimization should be possible, for example, by going to an entirely *in-situ* cleaning process. This edge formation process has also produced high quality HTS Josephson devices with ion-damaged YBCO layers serving as effective normal metal weak links. These ion-damage barrier devices have high current densities and I_cR_n products at 77 K, making thcm well-suited for superconducting device applications such as flux-quantum logic and SQUID magnetometers. However, this approach does have, some potential drawbacks. The critical current densities of the ion-damage weak links appear to be relatively insensitive to ion cleaning energy and ion species, indicating that J_c in these devices is not controllable over a wide range. This is a problem for some cases in which control of J_c is required, such as integrated circuit applications. In some other situations, however, the insensitivity of J_c to process variations could be a significant advantage. A second potential problem is that the device current densities are approaching the electrode J_c values, which can cause difficulties with electrode transitions unless care is taken to usc thick counterelectrodes. Finally, the R_nA products of the ion-damaged barrier weak

links are small, $R_nA \approx 5 \times 10^{-10}\ \Omega\text{-cm}^2$ at 4.2 K, so that 0.1 μm lithography will be required to produce 5 Ω devices.

N-YBCO WEAK LINKS

The edge formation and cleaning process just described provides the basis for fabrication of HTS weak links using deposited epitaxial normal metals. One possible SNS device technology uses a nonsuperconducting phase of $YBa_2Cu_3O_{7-x}$ (N-YBCO) as the normal metal. Some results on fabrication and testing of N-YBCO weak links have been presented previously (15, 16). Here we examine new data on N-YBCO characterization and N-YBCO device results, including the scaling behavior of the weak link critical current densities and I_cR_n products.

The N-YBCO thin films are deposited using a standard laser ablation process and a nearly stoichiometric $YBa_2Cu_3O_{7-x}$ target, except that the films are grown at ≈ 530 C, a much lower temperature than typically used to produce high quality superconducting YBCO thin films. Because of the difficulty of characterizing N-YBCO films deposited on the very small area YBCO base electrode edge, characterization of these films has been done primarily on N-YBCO layers grown directly on $LaAlO_3$ substrates, followed by a 1-2 minute anneal at ≈ 800 C, to mimic the counterelectrode growth conditions. Lateral transport resistivity measurements on 100 Å N-YBCO thin films grown in this manner show semiconductor-like behavior, although in some cases a drop in resistance is seen near 4 K. Resistivity measurements on much thicker N-YBCO films (3000 Å) show a superconducting transition at ≈ 40 K. X-ray diffraction studies of 500-1000 Å thick N-YBCO show peaks consistent with orthorhombic $YBa_2Cu_3O_{7-x}$ with a c-axis lattice constant of 11.68 Å. X-ray photoelectron spectroscopy (XPS) measurements on N-YBCO films produced with the above annealing procedure show no obvious difference from standard orthorhombic $YBa_2Cu_3O_{7-x}$. Finally, preliminary high resolution cross-sectional transmission electron microscopy (HRTEM) studies give images consistent with an orthorhombic YBCO phase.

These measurements demonstrate that N-YBCO is not the semiconducting cubic phase of YBCO reported by Agostinelli et al. (25). The characterization studies also indicate that N-YBCO is probably not the the nonsuperconducting oxygen-rich (26) or oxygen-poor (27) tetragonal phases reported earlier, because these phases exhibit c-axis lattice parameters smaller or larger than the value of 11.68 Å measured from the x-ray diffraction data. It appears most likely that N-YBCO is orthorhombic $YBa_2Cu_3O_{7-x}$ with oxygen disorder suppressing the transition temperature. A number of studies have shown that YBCO is especially susceptible to oxygen movement and that oxygen disorder can significantly affect T_c (24,28,29). Presumably, crystallization of the low-temperature-deposited YBCO film occurs during the heating ramp to the counterelectrode growth temperature, but sufficient oxygen disorder, and possibly other point defects remain to suppress superconductivity in these films. This supposition is consistent with device results indicating that SNS coupling through N-YBCO is sensitive to the high temperature counterelectrode growth parameters. In particular, we find that weak link current densities increase for hotter counterelectrode growth temperatures. These results suggest that N-YBCO is metastable, and that increased high temperature annealing results in reduced crystalline disorder and stronger weak link coupling. At room temperature, however, the N-YBCO devices are very stable, with almost no change in the current-voltage characteristics after more than a year of storage in an Ar-filled desiccator.

As reported previously (15,16), SNS weak links fabricated with N-YBCO normal metal layers typically exhibit RSJ-like current-voltage characteristics with some excess current. These devices show clean ac Josephson steps at 14.4 GHz, which modulate as expected with increasing microwave power. Studies of the magnetic 'field dependence of the critical currents in N-YBCO SNS weak links show Fraunhofer-like patterns with 30-90% modulation (16). This magnetic field behavior demonstrates good large scale barrier uniformity, but the incomplete modulation is consistent with fine scale nonuniforrnities in the N-YBCO or the N-S interfaces. Figure 5 is a plot of the average SNS weak link current density for the devices on 25 chips at 4.2 K as a function of the N-YBCO barrier thickness. The straight line is a fit to the data for N-YBCO thicknesses less than or equal to 100 Å, showing that J_c scales exponentially with barrier thickness in this range, with an effective normal metal coherence length of 23 Å. Devices with N-YBCO layers thicker than ≈ 100 Å suffer from degraded counterelectrode quality with lower transition temperatures and higher resistivities. For these devices, a more rapid decrease in J_c with increasing barrier thickness is seen due to the degradation of the counterelectrode properties. This deterioration in the quality of the YBCO counterelectrode suggests that there is an epitaxial growth problem on N-YBCO barriers over 100 Å, presumably because these layers are not providing a good epitaxial growth template for counterelectrode. overgrowth. This problem may be eliminated by more careful optimization of the N-YBCO growth and annealing conditions.

Another potential problem with these devices is the variation in device properties. Critical current density standard deviations across a single quarter inch chip were as small as 18%, and typically ranged from 20 - 100%. However, as much as an order of magnitude variation in critical currents was seen from chip to chip for a given barrier thickness, and the J_c standard deviations for all devices from all chips at each N-YBCO thickness ranged from ≈ 70% to 200%. Some of this variability can be attributed to process variations which were investigated during various device fabrication runs. In addition, the short coherence length and metastable nature of N-YBCO make these weak links especially susceptible to planned or unplanned process changes. Tighter process control is expected to help improve reproducibility.

We have also examined the scaling behavior of I_cR_n as a function of J_c for both the N-YBCO and ion-damage barrier devices, as shown in Figure 6. A fit to the data for $J_c < 10^5$ A/cm^2 indicates that I_cR_n scales as $J_c^{0.84}$ over a wide range of current densities. This scaling behavior is similar to that reported for grain boundary weak links and is evidence that transport in these devices occurs through superconducting filaments shunted by normal regions (24). Such nonuniform conduction could result from oxygen disorder in the N-YBCO layers or in the ion-damaged surface layer on the YBCO base electrode. This superconducting filament model is consistent with the magnetic field modulation studies of the critical currents, which pointed to fine scale nonuniformities in these devices. The second important point to note about the data of Figure 6 is that the I_cR_n products for most devices saturate at= 1-2 mV above 10^5 A/cm^2. This effect is probably due to self-shielding effects in these very high J_c devices. we calculate a Josephson penetration depth of= 1 μm at 10^5 A/cm^2 and our minimum device width is 1.5 μm. In fact, a replotting of the data (not shown) indicates that the smaller devices do have higher I_cR_n products at the highest current densities. We plan to fabricate smaller devices using electron beam lithography in an attempt to reproducibly obtain higher I_cR_n products. In addition, we are also examining other epitaxial normal metal layers such as $PrBa_2Cu_3O_{7-x}$ (18) in order to achieve improved weak link reproducibility and higher I_cR_n products at lower current densities.

SUMMARY

We have fabricated and tested HTS edge-geometry weak links utilizing ion-damaged YBCO and a nonsuperconducting phase of YBCO (N-YBCO) as weak link barrier materials. Special attention was focused on optimization of the YBCO base electrode edge formation and cleaning process. It was found that high quality YBCO edges could be prepared using a 500 eV Ar edge milling step in combination with 50 eV Ar cleaning. When used to fabricate weak links with no deposited barrier layer, in which the remnant ion damage serves as the weak link barrier, this cleaning process produced devices with average values of $J_c = 5.5 \times 10^4$ A/cm^2 and average R_nA products of 5.4×10^{-10} Ω-cm^2. The ion-damaged weak links exhibited good quality RSJ I-V characteristics, but could only be fabricated over a relatively limited current density range approaching the YBCO electrode J_c values. We have also produced SNS weak links using N-YBCO layers as the normal metal barrier. Characterization of the N-YBCO films suggests that this material is the orthorhombic phase of $YBa_2Cu_3O_{7-x}$ with oxygen disorder and possibly other point defects suppressing T_c. The N-YBCO weak links show RSJ I-V characteristics with strong microwave and magnetic field response. The critical currents of the N-YBCO devices scale exponentially with barrier thickness for barriers less than 100 Å with a nominal coherence length of 23 Å. The J_cR_n products of these devices are usually limited to 1-2 mV, and scale as $J_c^{0.84}$ in behavior similar to that reported for grain boundary junctions, suggesting that transport may be dominated by superconducting filaments shunted by normal regions. The I_cR_n scaling behavior also indicates that higher I_cR_n products may be obtained by fabricating smaller devices at the highest current densities.

AKNOWLEDGEMENTS

The research described in this paper was performed at the Center for Space Microelectronics Technology, Jet Propulsion Laboratory, California Institute of Technology, and was jointly sponsored by the Defense Advanced Research Projects Agency, the Strategic Defense Initiative Organization, Innovative Science and Technology Office, and the National Aeronautics and Space Administration, Office of Advanced Concepts and Technology.

REFERENCES

1. D.B. Schwartz, P.M. Mankiewich, R. Il. Howard, L.D. Jackel, B.L. Straughn, E.G. Burkhart, and A.H. Dayem, IEEE Trans. Magnetics 25, 1298 (1989).
2. M.G. Forrester, J. Talvacchio, J.R. Gavaler, M. Rooks, and J. Lindquist, IEEE Trans. Magnetics 27,3098 (1991).
3. M.S. Wire, R.W. Simon, J.A. Luine, K.P. Daly, S.B. Coons, A.E. Lee, R. Hu, J.F. Burch, and C.E. Platt, IEEE Trans. Magnetics 27,3106 (1991).
4. B Ghyselen, R. Cabanel, S. Tyc, D.G. Crete, Z.H. Barber, J.E. Evetts, G. Ben , Assayag, J. Gierak, and A. Schuhl, Physics C 198,215 (1992).
5. M.S. DiIorio, S. Yoshizumi, K-Y. Yang, M. Maung, J. Zhang, and B. Power, IEEE Trans. Applied Superconductivity 3,2011 (1993).
6. R.H. One, L.R. Vale, K.R. Kimminau, J.A. Bean, M.W. Cromar, C.D. Reintsema, T.E. Harvey, P.A. Rosenthal, and D.A. Rudman, IEEE Trans. Applied Superconductivity 3,2389 (1993).
7. P.A. Rosenthal, E.N. Grossman, R.H. One, and L.R. Vale, submitted to Applied Physics Letters (1993).

8. C.T. Rogers, A. Inam, M.S. Hegde, B. Dutta, X.D. Wu, and T. Venkatesan, Appl. Phys. Lett. 55,2032 (1989).
9. J.B. Barrier, C.T. Rogers, A. Inam, R. Ramesh, and S. Bersey, Appl. Phys. Lett. 59, 742 (1991).
10. K. Mizuno, K. Higashino, K. Setsune, and K. Wasa, Appl. Phys. Lett. 56, 1469 (1990).
11. G.F. Virshup, M.E. Klausmeier-Brown, I. Bozovic, and J.N. Eckstein, Appl. Phys. Lett. 60,2288 (1992).
12. T. Satoh, J. Fujita, T. Yoshitake, and H. Tsuge, Appl. Phys. Lett. 62, 1685 (1993).
13. R.B. Laibowitz, R.H. Koch, A. Gupta, G. Koren, W.J. Gallagher, V. Foglietti, B. Oh, and J. M. Viggiano, Appl. Phys. Lett. 56, 686 (1990).
14. G. Koren, E. Aharoni, E. Polturak, and D. Cohen, Appl. Phys. Lett. 58,634 (1991).
15. B.D. Hunt, M.C. Foote, and L.J. Bajuk, Appl. Phys. Lett. 59,982 (1991).
16. B. D. Hunt, L.J.Bajuk, J. B. Barrier, M.C. Foote, B. B. Jones, and R. P. Vasquez, SPIE Proceedings Vol. 1597: Progress in High Tc Superconducting Transistors and Other Devices II, 108 (1991).
17. Yu.M. Boguslavskij, J. Gao, A.J. Rijnders, D. Terpstra, G.J. Gerritsma, and H. Rogalla, Physics C 194,268 (1992).
18. J. B. Barrier, B. D. Hunt, W. T. Pike, M. C. Foote, and R. P. Vasquez, Physics C 207, 381 (1993).
19. K,Char, M. S.Colclough, T. H. Geballe, K. E. Myers, Appl. Phys. Lett. 62, 196 (1993).
20. J.A. Agostinelli, J.M. Chwalek, C.J. Baron, G. Lubberts, and C.D. Dowell, Physics C 207,203 (1993).
21. M.Y. Kupriyanov and K.K. Likharev, IEEE Trans. Magnetics 27,2460 (1991).
22. M.C. Foote, B.B. Jones, B.D. Hunt, J.B. Barrier, R.P. Vasquez and L.J. Bajuk, Physics C 201, 176 (10/92).
23. C. L.Jia, B. Kabius, K. Urban, K. Herrman, G.J. Cui, J. Schubert, W. Zander, and A.I. Braginski, Physics C 175,545 (1991).
24. B.H. Moeckly, D.K. Lathrop, and R.A. Buhrman, Phys. Rev. B 47,400 (1993).
25. J.A. Agostinelli, S. Chen, and G. Braunstein, Phys. Rev. B 43, 11396 (1991).
26. K.W. Lay, J. Am. Ceramics Sot. 72,696 (1989).
27. J.D. Jorgensen, B.W. Veal, A.P. Paulikas, L.J. Nowicki, G.W. Crabtree, H. Claus, and W.K. Kwok, Phys. Rev. B 41, 1863 (1990).
28. B. W. Veal, A. P.Paulikas, H.You, H.Shi, Y.Fang, J.W.Downey, Phys.Rev. B42, 6305.
29. R.J. Cava, A.W. Hewat, E.A. Hewat, B. Batlogg, M. Marezio, K.M. Rabe, J.J. Krajewski, W.F. Peck Jr., and L.W. Rupp Jr., Physics C 165,419 (1990).

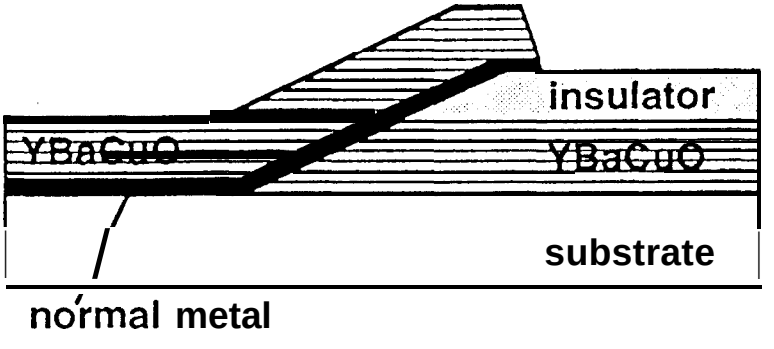

Figure 1. Cross-sectional schematic diagram of edge-geometry SNS weak link.

(a)

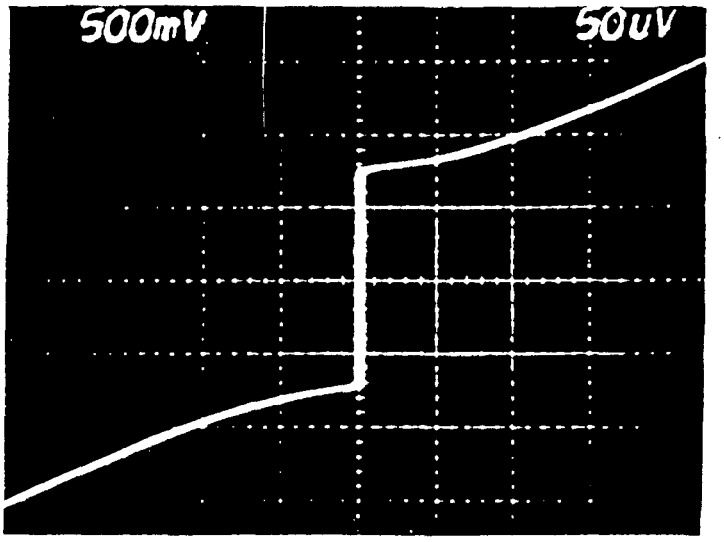

(b)

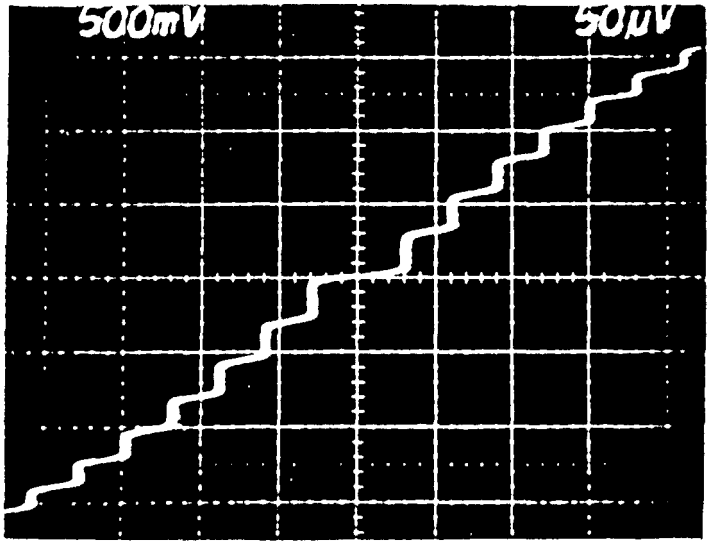

Figure 2. (a) Current-voltage characteristic at "-" K of damaged YBCO weak link produced by Ar-ion milling at 500 [illegible] with 50 eV Ar ions. The device size is 3 μm x [illegible] V, and R_nA =2.9x 10^{-9} Ω-cm^2. (b) Microwave [illegible] 4.4 GHz. For both I-Vs the vertical scale is [illegible] 'div.

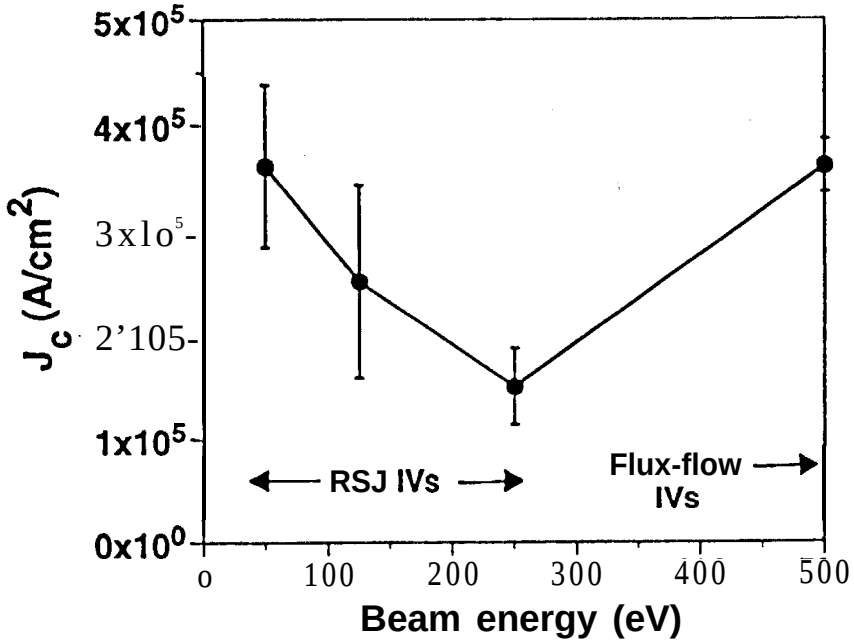

Figure 3. Plot of the average J_c versus Ar cleaning energy at 77 K for weak links on four chips produced with a 500 eV Ar edge cutting process and no deposited barrier layer. The error bars give the standard deviation in J_c for each chip.

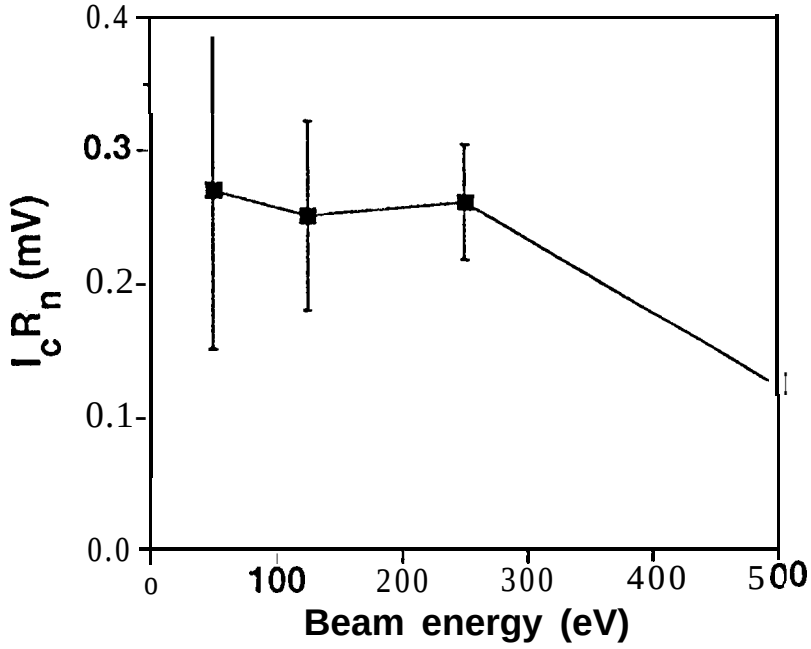

Figure 4. Plot of the average I_cR_n product versus Ar cleaning energy at 77 K for weak links on four chips produced with a 500 eV Ar edge cutting process and no deposited barrier layer. The error bars give the standard deviation in I_cR_n for each chip.

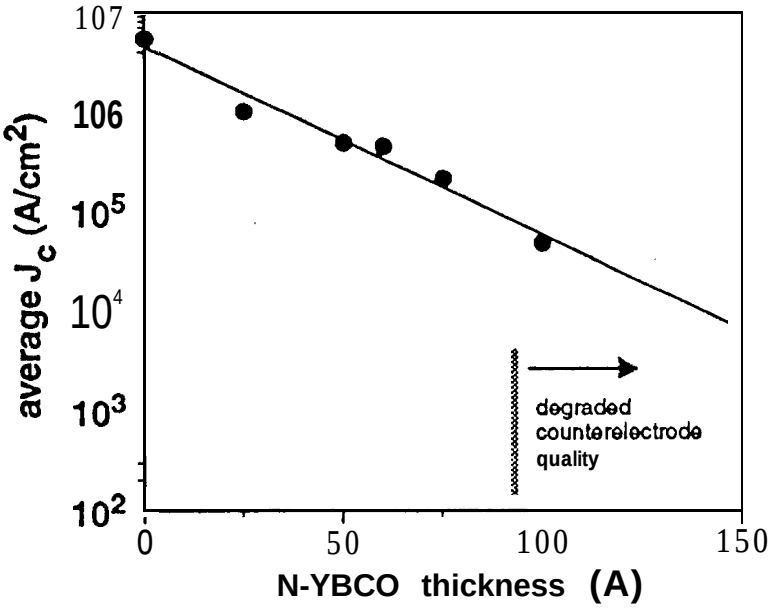

Figure 5. Plot of the average critical current density vs. N-YBCO thickness for 25 chips at 4.2 K. The line is a fit to $J_c = \exp(-L/\xi_n)$ for barrier thicknesses, L, less than or equal to 100 Å (solid points), and&=23 Å is the effective normal metal coherence length.

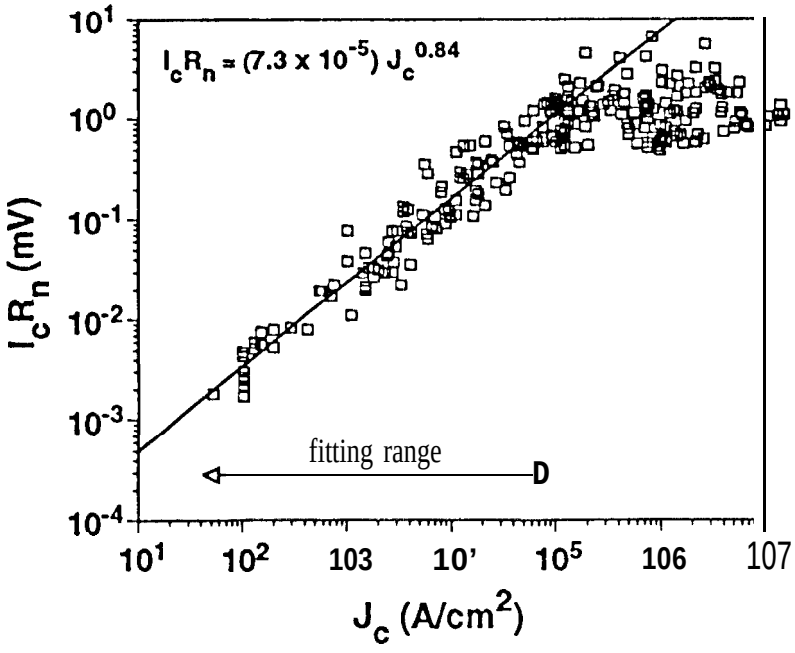

Figure 6. A plot of I_cR_n vs J_c for N-YBCO and ion-damage barrier devices on 33 chips at 4.2 K. The line is a fit to the data for $J_c < 10^5$ A/cm^2, indicating that I_cR_n scales as $J_c^{0.84}$ in this range.